Supporting Information

Efficient Oxygen Electrocatalysis by Nanostructured Mixed-Metal Oxides

Xiang-Kui Gu‡, Juliana S. A. Carneiro‡, Samji Samira, Anirban Das, Nuwandi M. Ariyasingha, and Eranda Nikolla*

Department of Chemical Engineering and Materials Science, Wayne State University, Detroit, MI 48202, United States

* Corresponding Author (erandan@wayne.edu)

‡ These authors contributed equally to this manuscript

1. DFT calculations and Microkinetic Modeling

The binding energy of oxygen is calculated as:

$$BE_O = E_{O/sur} - E_{sur} - (\frac{1}{2}E_{O_2} + \Delta h^0_{O_2}) \quad (1)$$

where $E_{O/sur}$, E_{sur}, and E_{O_2} are the total energies of the slab with O adsorbed, slab with a clean surface, and O_2 in gas phase, respectively. $\Delta h^0_{O_2}$ (0.48 eV) is the correction factor accounting for the overbinding of O_2 by DFT-GGA.[1]

The transition state of O_2 dissociation is located using the climbing-image nudged elastic band (CI-NEB) method.[2-3] The energy barrier (E_{TS}) is calculated with respect to O_2 in the gas phase using equation 2.

$$E_{TS} = E_{TS/sur} - E_{sur} - E_{O_2} + T\Delta S \quad (2)$$

$E_{TS/sur}$ represents the total energies of the transition state and slab. $T\Delta S$ is the entropic contribution. This leads to a 1.48 eV loss per O_2 molecule at an operating temperature of 500 ℃ and O_2 partial pressure of 0.21 atm, based on the reported calculated method.[4] During the DFT calculations, the spin of the system is allowed to relax for all images along the reaction coordinate to obtain reasonable barriers. This is important in obtaining an accurate magnetic moment for oxygen in adsorbed O_2, which increases gradually as the O-O bond is elongated. The spin flips observed have also been reported in the literature, and generally have shown to lead to accelerated reaction rates.[5-6]

Oxygen exchange between gas-phase O_2 and oxygen in solid oxides has been reported to occur through three different overall reactions based on the number of oxygen exchanged with the oxides.[7-12] One of these processes is known as homoexchange and involves the dissociation of two oxygen molecules on the surface and the exchange with each other, where no oxygen is exchanged

with the oxide lattice oxygen. This process generally proceeds at elevated temperatures and has minimum contribution from the oxides.[9] Therefore, it is not considered here. The heteroexchange process, which involves the exchange of gas-phase oxygen with one or two lattice oxygen of the oxide, is more appropriate at describing the surface oxygen exchange process on R-P oxides. To model this process using DFT, the following surface oxygen exchange mechanism, described by four elementary steps has been adopted (Figure S2)[13-15]:

$$O_O^X + V_i \rightarrow V_O^{\bullet\bullet} + O_i \qquad \text{s1}$$

$$O_2 + V_O^{\bullet\bullet} + * \rightarrow O* + O_O^X \qquad \text{s2}$$

$$O* + O_O^X \rightarrow O_2 + V_O^{\bullet\bullet} + * \qquad \text{s3}$$

$$O_i + V_O^{\bullet\bullet} \rightarrow O_O^X + V_i \qquad \text{s4}$$

where O_O^X is the surface lattice oxygen, V_i is a vacant interstitial site in the rock salt layer, O_i is an interstitial oxygen in the rock salt layer, $V_O^{\cdot\cdot}$ is an oxygen vacancy site on the surface layer. The first step is the generation of a surface oxygen vacancy via a surface lattice oxygen diffusion into an interstitial site. The second step involves the dissociation of gas-phase O_2 on this surface oxygen vacancy with one oxygen atom filling in the surface oxygen vacancy and the other one binding to the surface as an oxygen adatom. In the third step, evolution of the oxygen from the oxide to gas phase occurs via the oxygen adatom association with a surface lattice oxygen, leaving behind a surface oxygen vacancy. Lastly, the interstitial oxygen is transported to a surface oxygen vacancy to close the catalytic cycle. These four elementary steps can also be simply combined into two reversible steps:

$$O_O^X + V_i \underset{k_{-1}}{\overset{k_1}{\rightleftharpoons}} V_O^{\bullet\bullet} + O_i \qquad \text{s5}$$

$$O_2 + V_O^{\bullet\bullet} + * \underset{k_{-2}}{\overset{k_2}{\rightleftharpoons}} O* + O_O^X \qquad \text{s6}$$

A microkinetic modeling is used to calculate the rate of the surface oxygen exchange at 500 ℃ and O_2 pressure of 0.21 atm. The equilibrium and steady-state approximation is used to determine the coverage of intermediates and the vacant active sites:

$$k_1\theta_{O_O^x}\theta_{V_i} = k_{-1}\theta_{O_i}\theta_{V_O^{\bullet\bullet}} \tag{3}$$

$$k_2\theta_*\theta_{V_O^{\bullet\bullet}}P_{O_2} = k_{-2}\theta_{O^*}\theta_{O_O^x} \tag{4}$$

$$\theta_{O_O^x} + \theta_{V_O^{\bullet\bullet}} = 1 \tag{5}$$

$$\theta_{O^*} + \theta_* = 1 \tag{6}$$

$$\theta_{V_i} + \theta_{O_i} = 1 \tag{7}$$

$$\theta_{O_i} - \theta_{V_O^{\bullet\bullet}} = 0 \tag{8}$$

The coverages of surface oxygen vacancy ($\theta_{V_O^{\bullet\bullet}}$) and oxygen adatom (θ_{O^*}) are expressed as:

$$\theta_{V_O^{\bullet\bullet}} = \frac{k_1 - \sqrt{k_1 k_{-1}}}{k_1 - k_{-1}} \tag{9}$$

$$\theta_{O^*} = \frac{k_2\theta_{V_O^{\bullet\bullet}}P_{O_2}}{k_2\theta_{V_O^{\bullet\bullet}}P_{O_2} + k_{-2}(1-\theta_{V_O^{\bullet\bullet}})} = \frac{1}{1+\frac{k_{-2}(1-\theta_{V_O^{\bullet\bullet}})}{k_2\theta_{V_O^{\bullet\bullet}}P_{O_2}}} \tag{10}$$

The rate constant (k) for each elementary step is calculated using equation 11[16]:

$$k = \frac{k_b T}{h}\exp(-E_a / RT) \tag{11}$$

where k_b, h, *and* E_a are the Boltzmann constant, Planck constant, and activation barrier, respectively. We note that E_a is an effective barrier involving the entropic contribution for the adsorption/desorption steps, as shown in equation 2.

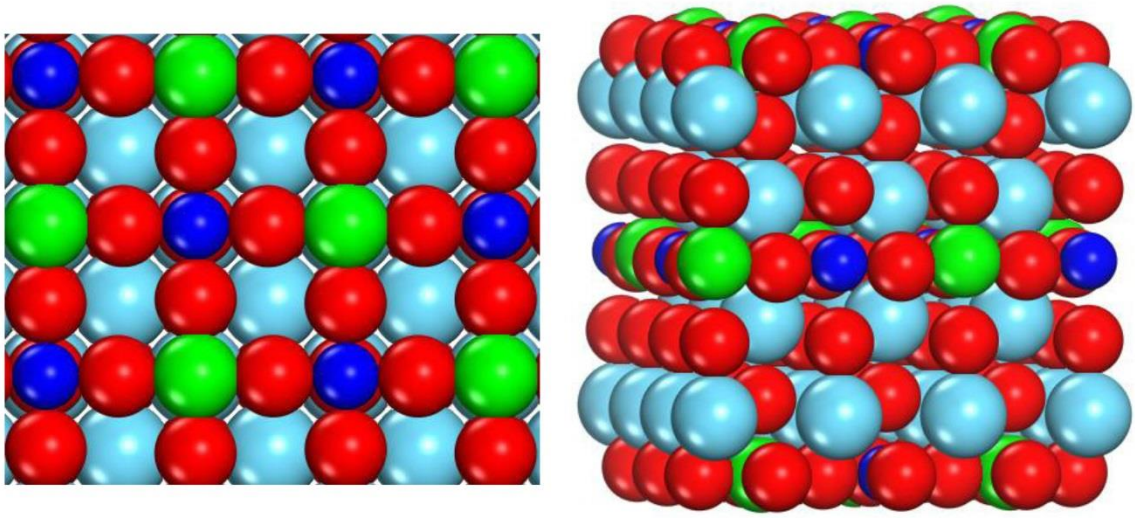

Figure S1. The structures of B-site terminated (001) surfaces for first-series R-P oxides with mixed B-site transition metals. The cyan, green/blue, and red spheres represent La, transition metal, and O atoms, respectively.

The exact distribution of the dopant per atomic layer in R-P oxides is difficult to predict theoretically due to the large number of possible structures. To theoretically determine the dopant effect on the activity, a homogenous distribution is considered to assure that all the oxides have the same geometric structure. This allows for a systematic link between the chemical composition and activity of these oxides on geometrically similar sites. The general distribution of the B-site metals in the structure is supported by our EDS line scan data, which shows homogeneous-like distribution of the B-site elements in the nanostructures of the different oxides (Figures S6-9).

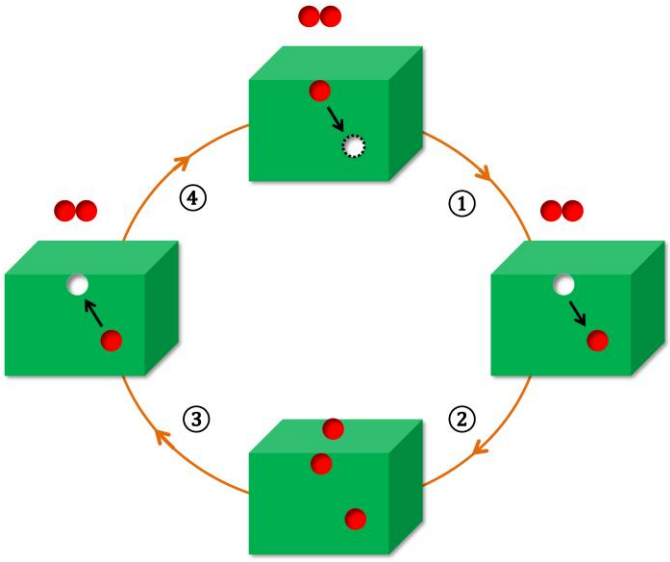

Figure S2. Proposed mechanism for surface oxygen exchange on first-series R-P oxides. Red, dashed white, and white spheres represent the O atoms, vacant interstitial sites, and surface oxygen vacancies, respectively.

2. Oxygen Isotopic Exchange Model

Oxygen exchange has been reported to occur via a heteroexchange of gas phase oxygen with oxygen in the non-stoichiometric mixed ionic-electronic conducting oxides.[8, 11] The heteroexchange process for surface oxygen exchange between isotopic labeled $^{18}O_2$ and the oxygen in R-P oxides can be described using reactions r1-r4:

$$^{18}O_2 + {}^{16}O_i \rightleftharpoons {}^{16}O{}^{18}O + {}^{18}O_i \quad \text{r1}$$

$$^{16}O_2 + {}^{18}O_i \rightleftharpoons {}^{16}O{}^{18}O + {}^{16}O_i \quad \text{r2}$$

$$^{16}O{}^{18}O + {}^{16}O_O^X \rightleftharpoons {}^{16}O_2 + {}^{18}O_O^X \quad \text{r3}$$

$$^{16}O{}^{18}O + {}^{18}O_O^X \rightleftharpoons {}^{18}O_2 + {}^{16}O_O^X \quad \text{r4}$$

The corresponding elementary steps involved in these reactions are described using steps s7-s12:

$$^{16}O_O^X + V_i \underset{k_{-1}}{\overset{k_1}{\rightleftharpoons}} V_O^{\bullet\bullet} + {}^{16}O_i \quad \text{s7}$$

$$^{18}O_O^X + V_i \underset{k_{-1}}{\overset{k_1}{\rightleftharpoons}} V_O^{\bullet\bullet} + {}^{18}O_i \quad \text{s8}$$

$$^{18}O_2 + V_O^{\bullet\bullet} + * \underset{k_{-2}}{\overset{k_2}{\rightleftharpoons}} {}^{18}O* + {}^{18}O_O^X \quad \text{s9}$$

$$^{16}O_2 + V_O^{\bullet\bullet} + * \underset{k_{-2}}{\overset{k_2}{\rightleftharpoons}} {}^{16}O* + {}^{16}O_O^X \quad \text{s10}$$

$$^{16}O* + {}^{18}O_O^X \underset{k_2}{\overset{k_{-2}}{\rightleftharpoons}} {}^{16}O{}^{18}O + V_O^{\bullet\bullet} + * \quad \text{s11}$$

$$^{18}O* + {}^{16}O_O^X \underset{k_2}{\overset{k_{-2}}{\rightleftharpoons}} {}^{16}O{}^{18}O + V_O^{\bullet\bullet} + * \quad \text{s12}$$

The expressions for the coverages of the oxygen species, surface oxygen vacant site, and interstitial vacant site are obtained by assuming equilibrium between the surface and bulk oxygen (steps s7-s8), and steady state approximation for all the other elementary steps (s9-s12). Based on these assumptions, the following expressions are obtained:

$$k_1\theta_{^{16}O_O^x}\theta_{V_i} = k_{-1}\theta_{^{16}O_i}\theta_{V_O^{\bullet\bullet}} \quad (12)$$

$$k_1\theta_{^{18}O_O^x}\theta_{V_i} = k_{-1}\theta_{^{18}O_i}\theta_{V_O^{\bullet\bullet}} \quad (13)$$

$$d\theta_{V_i}/dt = k_{-1}\theta_{^{16}O_i}\theta_{V_O^{\bullet\bullet}} + k_{-1}\theta_{^{18}O_i}\theta_{V_O^{\bullet\bullet}} - k_1\theta_{^{16}O_O^x}\theta_{V_i} - k_1\theta_{^{18}O_O^x}\theta_{V_i} = 0 \quad (14)$$

$$d\theta_{^{16}O^*}/dt = k_2 C_{^{16}O_2}\theta_*\theta_{V_O^{\bullet\bullet}} + k_2 C_{^{16}O^{18}O}\theta_*\theta_{V_O^{\bullet\bullet}} - k_{-2}\theta_{^{16}O^*}\theta_{^{16}O_O^x} - k_{-2}\theta_{^{16}O^*}\theta_{^{18}O_O^x} = 0 \quad (15)$$

$$d\theta_{^{18}O^*}/dt = k_2 C_{^{18}O_2}\theta_*\theta_{V_O^{\bullet\bullet}} + k_2 C_{^{16}O^{18}O}\theta_*\theta_{V_O^{\bullet\bullet}} - k_{-2}\theta_{^{18}O^*}\theta_{^{18}O_O^x} - k_{-2}\theta_{^{18}O^*}\theta_{^{16}O_O^x} = 0 \quad (16)$$

$$d\theta_{^{16}O_O^x}/dt = k_{-1}\theta_{^{16}O_i}\theta_{V_O^{\bullet\bullet}} + k_2 C_{^{16}O^{18}O}\theta_*\theta_{V_O^{\bullet\bullet}} + k_2 C_{^{16}O_2}\theta_*\theta_{V_O^{\bullet\bullet}} - k_1\theta_{^{16}O_O^x}\theta_{V_i} - k_{-2}\theta_{^{16}O^*}\theta_{^{16}O_O^x} - k_{-2}\theta_{^{18}O^*}\theta_{^{16}O_O^x} = 0 \quad (17)$$

$$d\theta_{^{18}O_O^x}/dt = k_{-1}\theta_{^{18}O_i}\theta_{V_O^{\bullet\bullet}} + k_2 C_{^{16}O^{18}O}\theta_*\theta_{V_O^{\bullet\bullet}} + k_2 C_{^{18}O_2}\theta_*\theta_{V_O^{\bullet\bullet}} - k_1\theta_{^{18}O_O^x}\theta_{V_i} - k_{-2}\theta_{^{16}O^*}\theta_{^{18}O_O^x} - k_{-2}\theta_{^{18}O^*}\theta_{^{18}O_O^x} = 0 \quad (18)$$

where $C_{^{16}O_2}$, $C_{^{16}O^{18}O}$, and $C_{^{18}O_2}$ are the concentrations of $^{16}O_2$, $^{16}O^{18}O$, and $^{18}O_2$, respectively. The measured partial pressures are converted to concentrations using ideal gas law ($C_i = \frac{p_i}{RT}$; where C_i is defined as $\frac{n_i}{V}$). The following site balances are used assuming that all sites are energetically equivalent:

$$\theta_{^{16}O_O^x} + \theta_{^{18}O_O^x} + \theta_{V_O^{\bullet\bullet}} = 1 \quad (19)$$

$$\theta_{^{16}O_i} + \theta_{^{18}O_i} + \theta_{V_i} = 1 \quad (20)$$

$$\theta_{^{16}O_i} + \theta_{^{18}O_i} = \theta_{V_O^{\bullet\bullet}} \quad (21)$$

$$\theta_{^{16}O^*} + \theta_{^{18}O^*} + \theta_* = 1 \quad (22)$$

Based on equations 12-22, the coverages of the surface oxygen vacancy ($\theta_{V_O^{\bullet\bullet}}$), lattice oxygen ($\theta_{^{16}O_O^x}$ and $\theta_{^{18}O_O^x}$), and adsorbed oxygen ($\theta_{^{16}O^*}$ and $\theta_{^{18}O^*}$) can be determined using equations 23-28:

$$\theta_{V_O^{\bullet\bullet}} = \frac{k_1 - \sqrt{k_1 k_{-1}}}{k_1 - k_{-1}} \quad (23)$$

$$\theta_* = \frac{k_{-2}(1-\theta_{V_O^{\bullet\bullet}})}{k_2\theta_{V_O^{\bullet\bullet}}(C_{^{16}O_2} + 2C_{^{16}O^{18}O} + C_{^{18}O_2}) + k_{-2}(1-\theta_{V_O^{\bullet\bullet}})} \quad (24)$$

$$\theta_{^{16}O^*} = \frac{k_2\theta_*\theta_{V_O^{\bullet\bullet}}(C_{^{16}O_2} - C_{^{18}O_2}) + k_{-2}(1-\theta_{V_O^{\bullet\bullet}})(1-\theta_*)}{2k_{-2}(1-\theta_{V_O^{\bullet\bullet}})} \quad (25)$$

$$\theta_{^{18}O^*} = 1-\theta_* - \theta_{^{16}O^*} \quad (26)$$

$$\theta_{^{16}O_O^X} = \frac{k_2\theta_*\theta_{V_O^{\bullet\bullet}}(C_{^{16}O^{18}O} + C_{^{16}O_2})}{k_{-2}(1-\theta_*)} \quad (27)$$

$$\theta_{^{18}O_O^X} = 1-\theta_{V_O^{\bullet\bullet}} - \theta_{^{16}O_O^X} \quad (28)$$

At a given temperature, the rates of $^{16}O_2$, $^{16}O^{18}O$, and $^{18}O_2$ can be determined using equations 29-31:

$$r_{^{16}O_2} = k_{-2}\theta_{^{16}O^*}\theta_{^{16}O_O^X} - k_2C_{^{16}O_2}\theta_*\theta_{V_O^{\bullet\bullet}} \quad (29)$$

$$r_{^{18}O_2} = k_{-2}\theta_{^{18}O^*}\theta_{^{18}O_O^X} - k_2C_{^{18}O_2}\theta_*\theta_{V_O^{\bullet\bullet}} \quad (30)$$

$$r_{^{16}O^{18}O} = k_{-2}\theta_{^{16}O^*}\theta_{^{18}O_O^X} + k_{-2}\theta_{^{18}O^*}\theta_{^{16}O_O^X} - 2k_2C_{^{16}O^{18}O}\theta_*\theta_{V_O^{\bullet\bullet}} \quad (31)$$

To model the transient curves for $^{16}O_2$, $^{16}O^{18}O$, and $^{18}O_2$ generated from oxygen exchange in a plug flow reactor, the following governing equation is used:

$$\frac{\partial C_i}{\partial t} = -u\frac{\partial C_i}{\partial z} + \frac{\rho_B}{\varepsilon}r_i \quad (32)$$

where C_i is the concentration of species i (i = $^{16}O_2$, $^{18}O_2$ and $^{16}O^{18}O$). The following boundary conditions are based on the isotopic switch from $^{16}O_2$ to $^{18}O_2$:

I. z = 0, $C_i = C_i^0$

II. z = L, $\left[\frac{\partial C_i}{\partial z}\right]_{z=L} = 0$

where L is the axial length of the catalyst bed. Based on these boundary conditions, equation 32 is solved numerically to obtain the concentration (or partial pressure) of the species i at each time on MATLAB® using Levenberg-Marquardt non-linear least squares regression algorithm. During the calculations, the values for the pre-exponential factors and activation energies are solved using an initial guess value (resulting in k_2, and k_{-2} values, accordingly) for steps s9-s12 considering both forward and reverse reactions. In the case of steps s7-s8, only the forward reaction parameters are solved to obtain k_1. To determine k_{-1}, the equilibrium constant for steps s7-s8 is used as shown below:

$$K_{eq} = \frac{(\theta_{^{16}O_i} + \theta_{^{18}O_i})\theta_{V_O^{\bullet\bullet}}}{(\theta_{^{16}O_O^X} + \theta_{^{18}O_O^X})\theta_{V_i}} = \frac{\theta_{O_i}\theta_{V_O^{\bullet\bullet}}}{\theta_{O_O^X}\theta_{V_i}} = \frac{\theta_{O_i}^2}{(1-\theta_{O_i})^2} \quad (33)$$

$$k_{-1} = \frac{k_1}{K_{eq}} = \frac{k_1(1-\theta_{O_i})^2}{\theta_{O_i}^2} \quad (34)$$

K_{eq} can be estimated from the concentration of the interstitial oxygen, δ, in these R-P oxides, which is experimentally determined using iodometric titrations.[17] Given the challenge with determining accurately the value of δ under equilibrium conditions, we have adopted a method where the oxide undergoes oxygen exchange at 500°C, followed by rapid cooling to room temperature to obtain the δ values.[18-19] The catalyst samples are then dissolved in HCl, followed by addition of KI solution in an N_2 saturated environment. This is titrated against a solution of 0.02 N sodium thiosulfate using starch solution as the indicator. The concentration of interstitial oxygen in Fe-LNO, Co-LNO, LNO, and Cu-LNO is determined to be 0.15 ± 0.02, 0.12 ± 0.02, 0.11 ± 0.02, and 0.10 ± 0.03, respectively.

In the model fitting process, the sum-squared error (SSE) is minimized between the data obtained from the model (X^{model}) calculated from equation 32 and the experimental data ($X^{exp.}$).

$$SSE = \sum_{i=1}^{n} (X_i^{\text{exp.}} - X_i^{\text{model}})^2 \quad (35)$$

To determine SSE, only the exchanged $^{18}O_2$ is used, which is obtained from the $^{18}O_2$ concentration at the beginning of the isotope switch.[8] For example, in the case of oxygen exchange on Co-LNO at 450 °C, the initial $^{18}O_2$ partial pressure is 0.017 atm, suggesting that ~ 10 % of the inlet $^{18}O_2$ is participating in the exchange process (Figure 4 in the main text).

3. Synthesis of Nanostructured R-P oxides

As an example, we discuss the detailed method used to prepare $La_2Ni_{0.88}Co_{0.12}O_{4+\delta}$. Into two separate round bottom flasks, ~0.03 mol cetyltrimethylammonium bromide (CTAB), 11 ml n-butanol, and 56 ml hexanes are added. The base and the metal salt solutions are prepared in de-ionized water in two separate vials. The base solution is prepared by dissolving ~0.02 mol KOH in 5.6 ml de-ionized water. The metal salt solution is prepared by dissolving 4 mmol $La(NO_3)_3 \cdot 6H_2O$ (99.999%, Sigma Aldrich), 1.75 mmol $Ni(NO_3)_2 \cdot 6H_2O$ (98%, Alpha Aesar), and 0.2 mmol $Co(NO_3)_2 \cdot 6H_2O$ (99.999%, Sigma Aldrich) in 0.8 ml de-ionized water. The base solution is added to one of the round bottom flasks and the metal salt solution is added to the other one. Vigorous stirring and intermittent ultrasonic treatments are carried out to obtain a transparent microemulsion suspension in each flask. Thereafter, the two microemulsions are mixed and stirred at 1100 rpm for 4 hours. The resulting gel is separated from the suspension by centrifugation (8000 rpm, 3 min) and washed with ethanol (3 times, 35 ml each time) and then de-ionized water (3 times, 35 ml each time). Each washing comprised of adding an appropriate solvent, mixing and intermittent ultrasonic treatment to disperse the solids and subsequent centrifugation at 8000 rpm for 3 minutes. The rest of the nanostructured R-P oxides are prepared by an analogous method. The obtained solids are all dried for 12 hours at 80 ℃ and calcined under an Ar flow at 825-925 ℃.

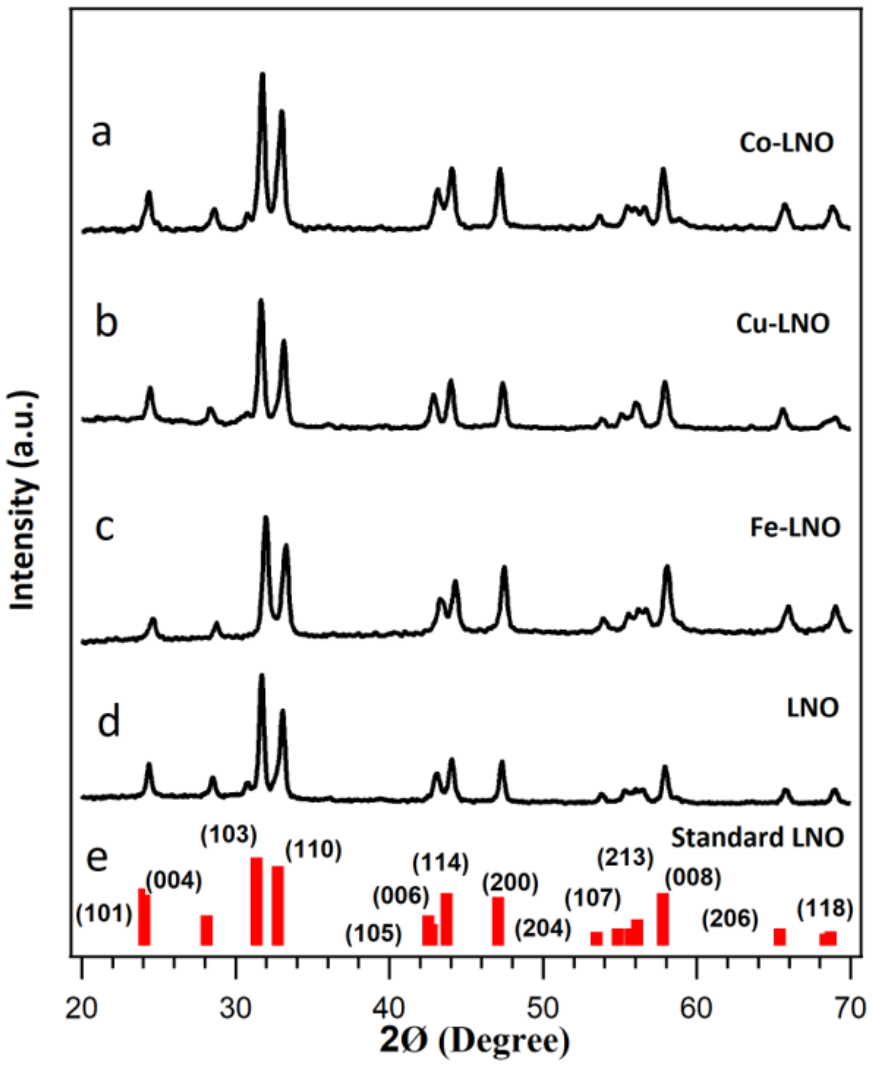

Figure S3. Powder XRD spectra for a) Co-LNO, b) Cu-LNO, c) Fe-LNO, d) LNO, and e) standard bulk LNO (JCPDS No. 34-0314). All XRD data here and thereafter are collected on a Bruker Phase II diffractometer with a Cu radiation source operating at 30kV, 10 mA, and equipped with a LYNXEYE detector.

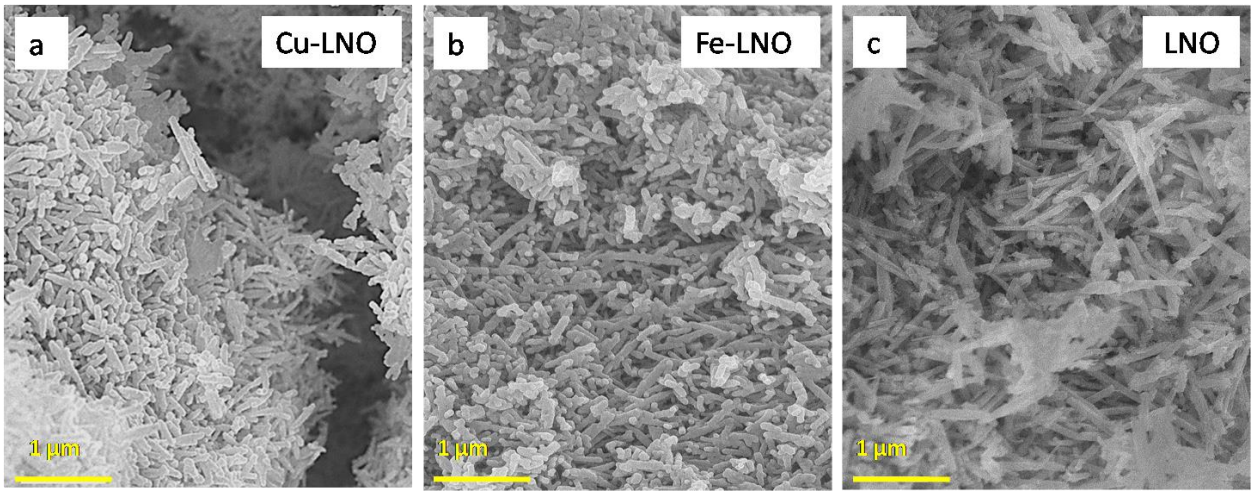

Figure S4. SEM images of a) Cu-LNO, b) Fe-LNO, and c) LNO as synthesized. Similar to Co-LNO shown in the main text, uniform, nanorod morphologies are also observed for these oxides.

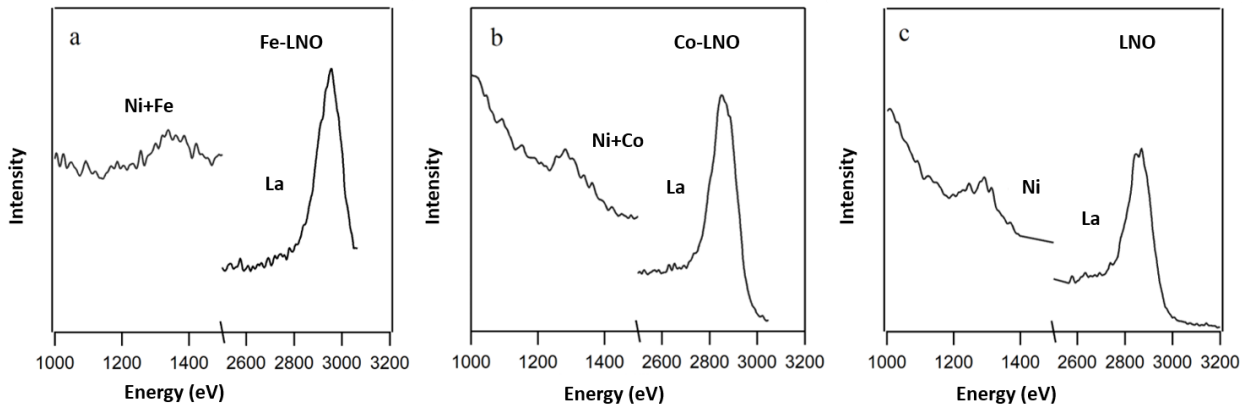

Figure S5. LEIS spectra for a) Fe-LNO, b) Co-LNO, and c) LNO.

LEIS spectra are collected after a dose of 0.5 $x10^{15}$ ions cm^{-2} of 0.5 keV Ar^{+}. For all the oxides, the La peak appears at ~2875 eV and the Ni appears at ~1250 eV. Slightly broader peaks for the mixed B-site transition metals are found on both Fe-LNO and Co-LNO, which can be attributed to the effect of the dopant peaks overlapping with Ni.

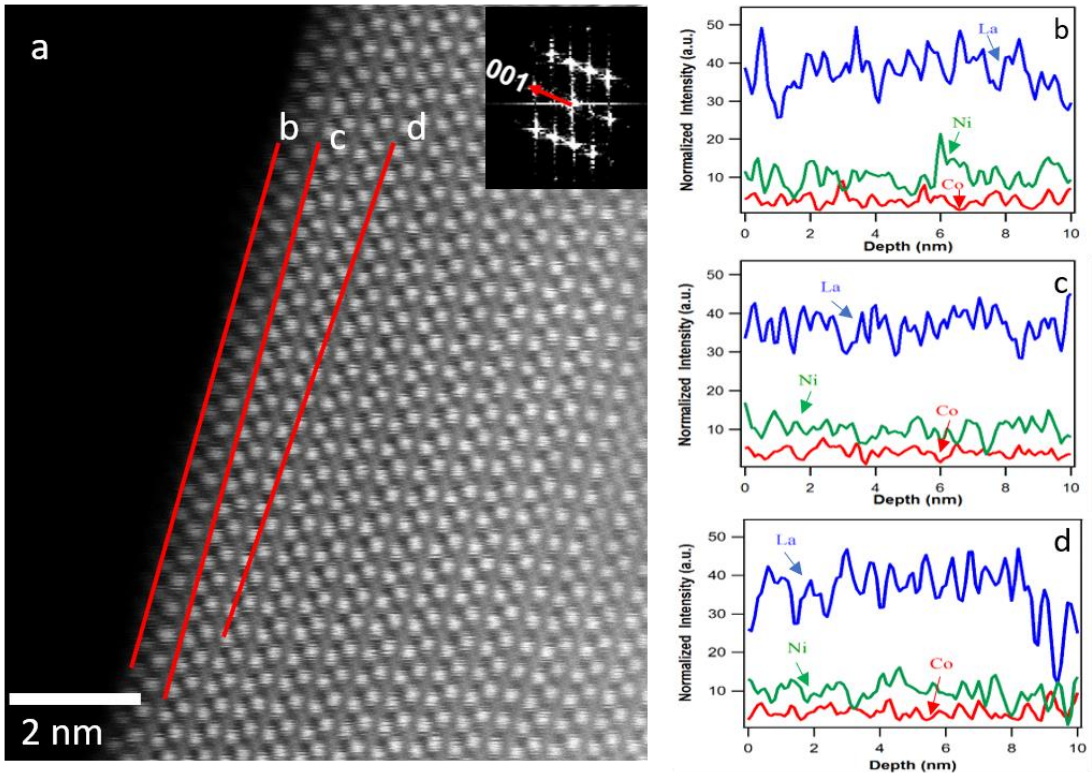

Figure S6. STEM/EDS characterization of Co-LNO nanorods for three different regions indicated by b, c, and d line scans. The HR-STEM image clearly shows the surface structure of Co-LNO nanorod with the layered R-P oxide structure. Three different line scans (b, c, and d) along the surface of the nanorod are conducted and the normalized intensities of La, Ni and Co are plotted on the right. These results show that: (i) Ni and Co are both present in the surface layer suggesting the B-site termination of the surface, and (ii) Co is uniformly distributed throughout the structure.

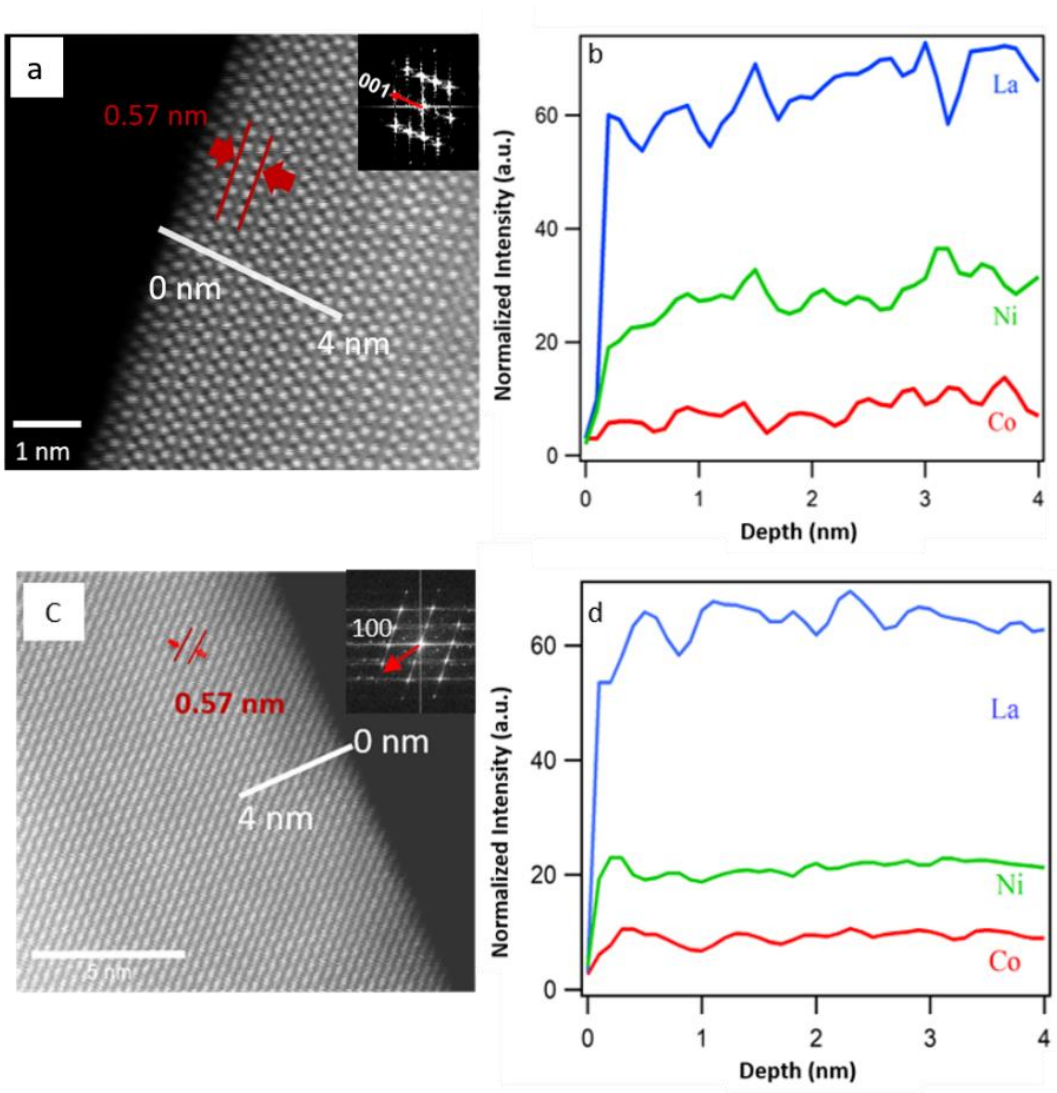

Figure S7. Pre- and post-reaction STEM/EDS characterization of Co-LNO nanorods. a) STEM image of the as-synthesized Co-LNO before the reaction along with the line used for EDS scanning. b) Normalized intensities of La, Ni, and Co for the indicated EDS line scan in a. c) STEM image of Co-LNO after the reaction and d) the elemental distribution along the EDS line scan in c. The projection axis and the FFT patterns of the TEM images of a and c are indicated as insets.

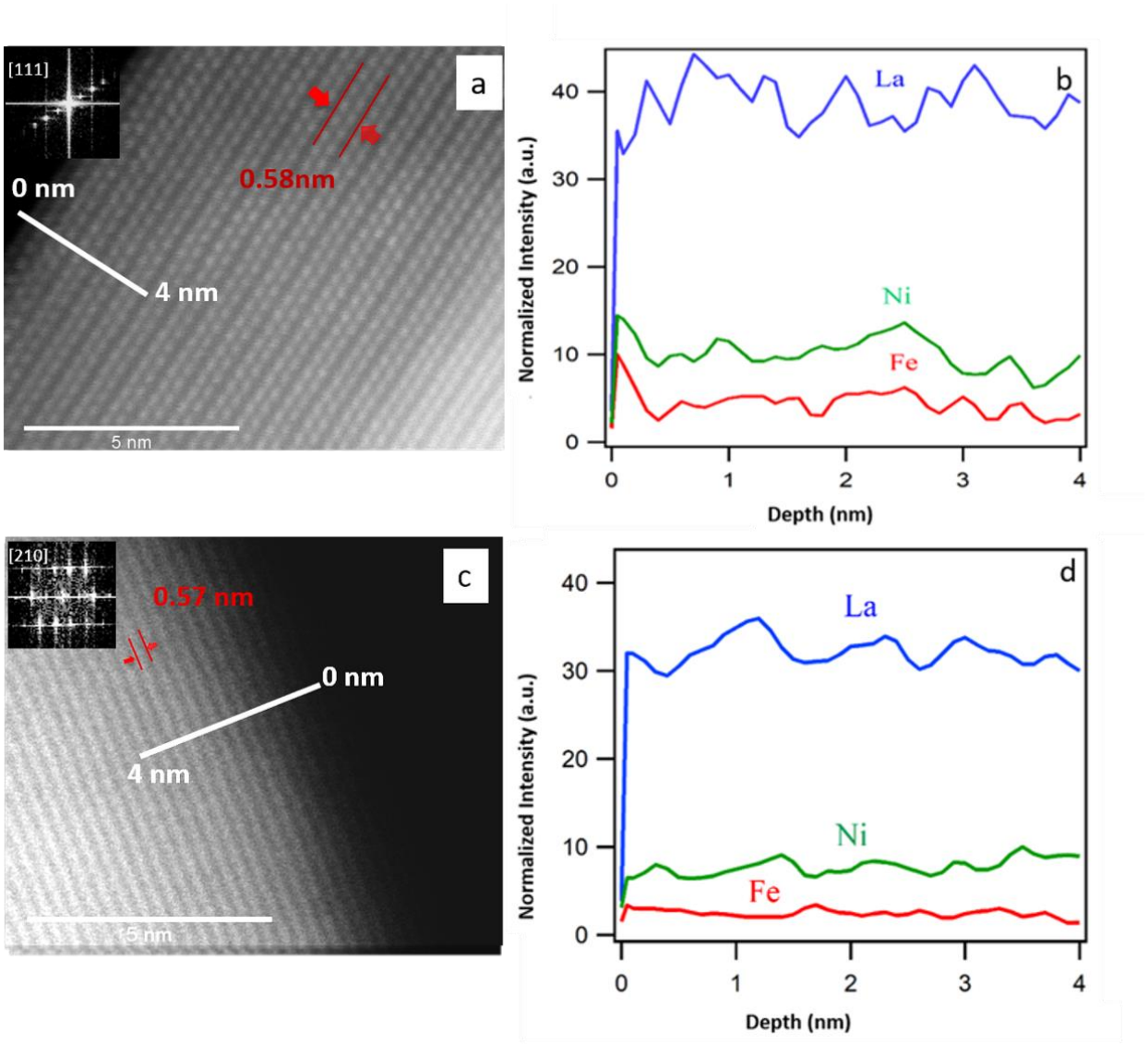

Figure S8. Pre- and post-reaction STEM/EDS characterization of Fe-LNO nanorods. a) STEM image of the as-synthesized Fe-LNO before the reaction along with the line used for EDS scanning. b) Normalized intensities of La, Ni, and Fe for the indicated EDS line scan in a. c) STEM image of Fe-LNO after the reaction and d) the elemental distribution along the EDS line scan in c.

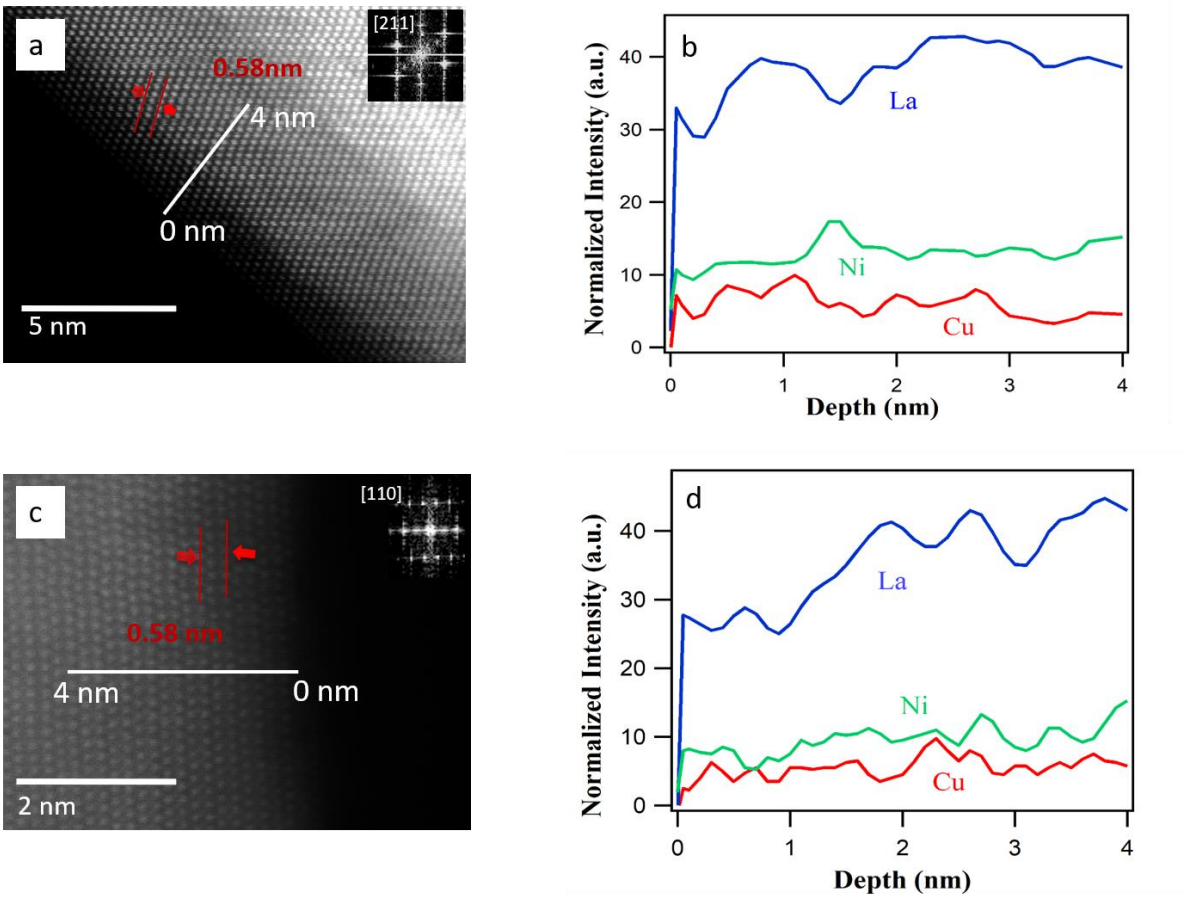

Figure S9. Pre- and post-reaction STEM/EDS characterization of Cu-LNO nanorods. a) STEM image of the as-synthesized Cu-LNO before the reaction along with the line used for EDS scanning. b) Normalized intensities of La, Ni, and Cu for the indicated EDS line scan in a. c) STEM image of Cu-LNO after the reaction and d) the elemental distribution along the EDS line scan in c.

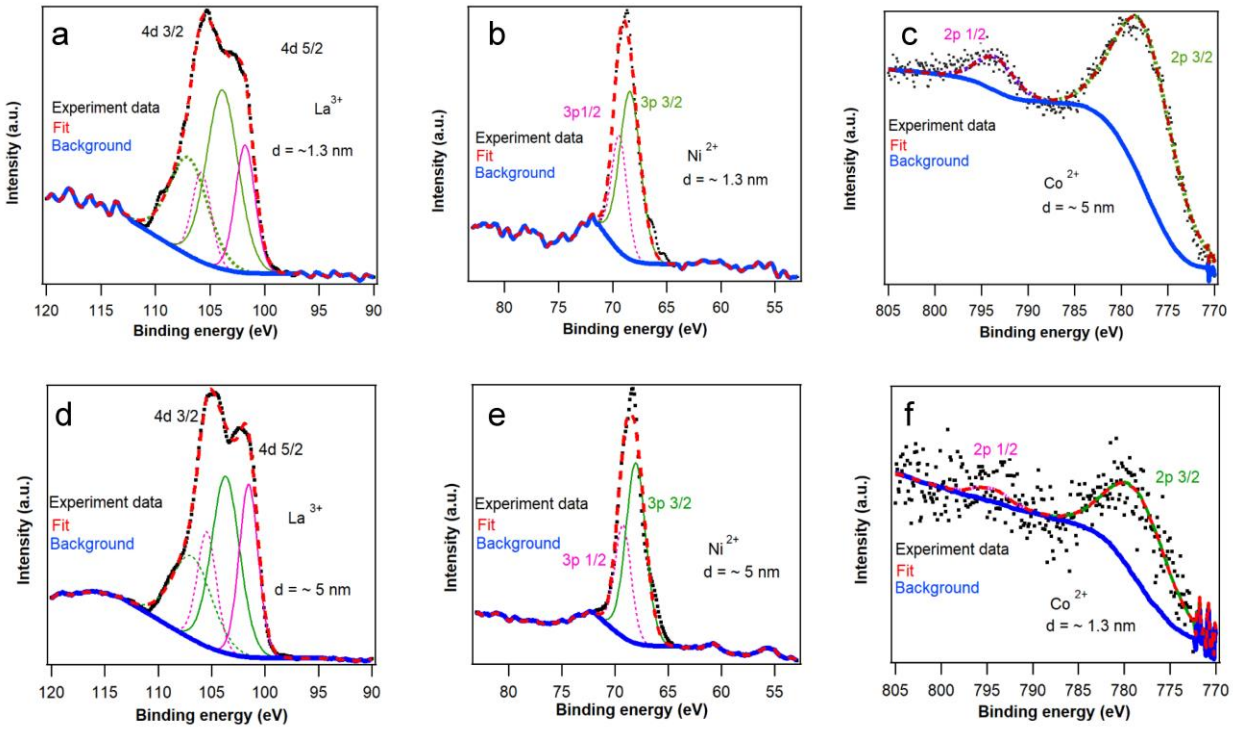

Figure S10. AR-XPS spectra of La, Ni, and Co for Co-LNO collected at 0° and 80° tilt angle with respect to the normal surface at 0°. The corresponding detected depths are ~5.0 and 1.3 nm.[20] The solid lines represent 4d 5/2, 3p 3/2, and 2p 3/2, while the dotted lines represent 4d 3/2, 3p1/2, and 2p 1/2 for La, Ni, and Co, respectively. La spectra (a and d) show two different peaks due to spin orbit coupling.[21] The oxidation states are calculated based on the binding energy data given in the NIST XPS website and from previous reported studies on La^{3+}, Ni^{2+}, and Co^{2+} oxides.[22-28] The observed oxidation states of La^{3+}, Ni^{2+}, and Co^{2+} at both depths are consistent with that in the R-P structure, suggesting that Co dopants are uniformly distributed in Co-LNO without reconstructing at the near surface.

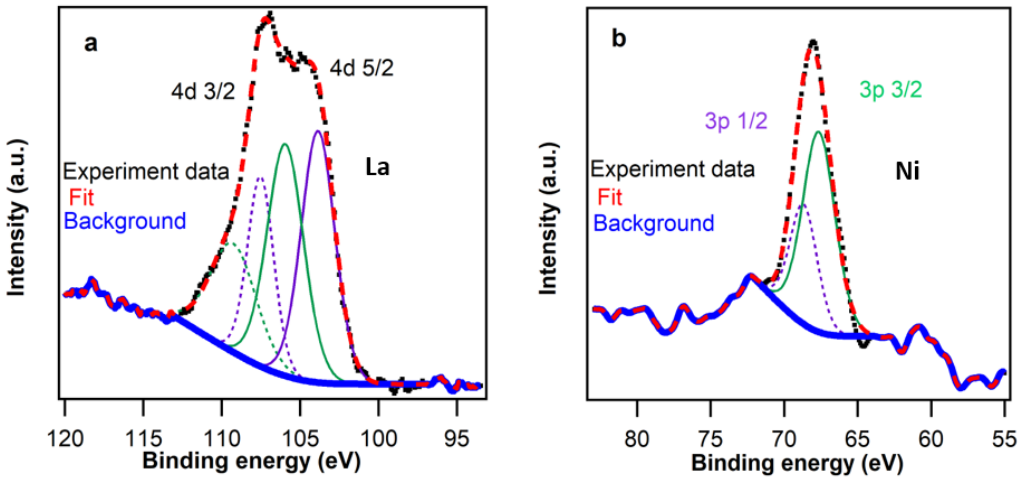

Figure S11. XPS spectra of La and Ni for LNO. The solid lines represent 4d 5/2 (La) and 3p 1/2 (Ni), while the dotted lines represent 4d 3/2 (La) and 3p3/2 (Ni). The two different peaks for La spectra stem from the spin orbit coupling.[21] The oxidation states of La^{3+} and Ni^{2+} are consistent with that in the R-P structure.

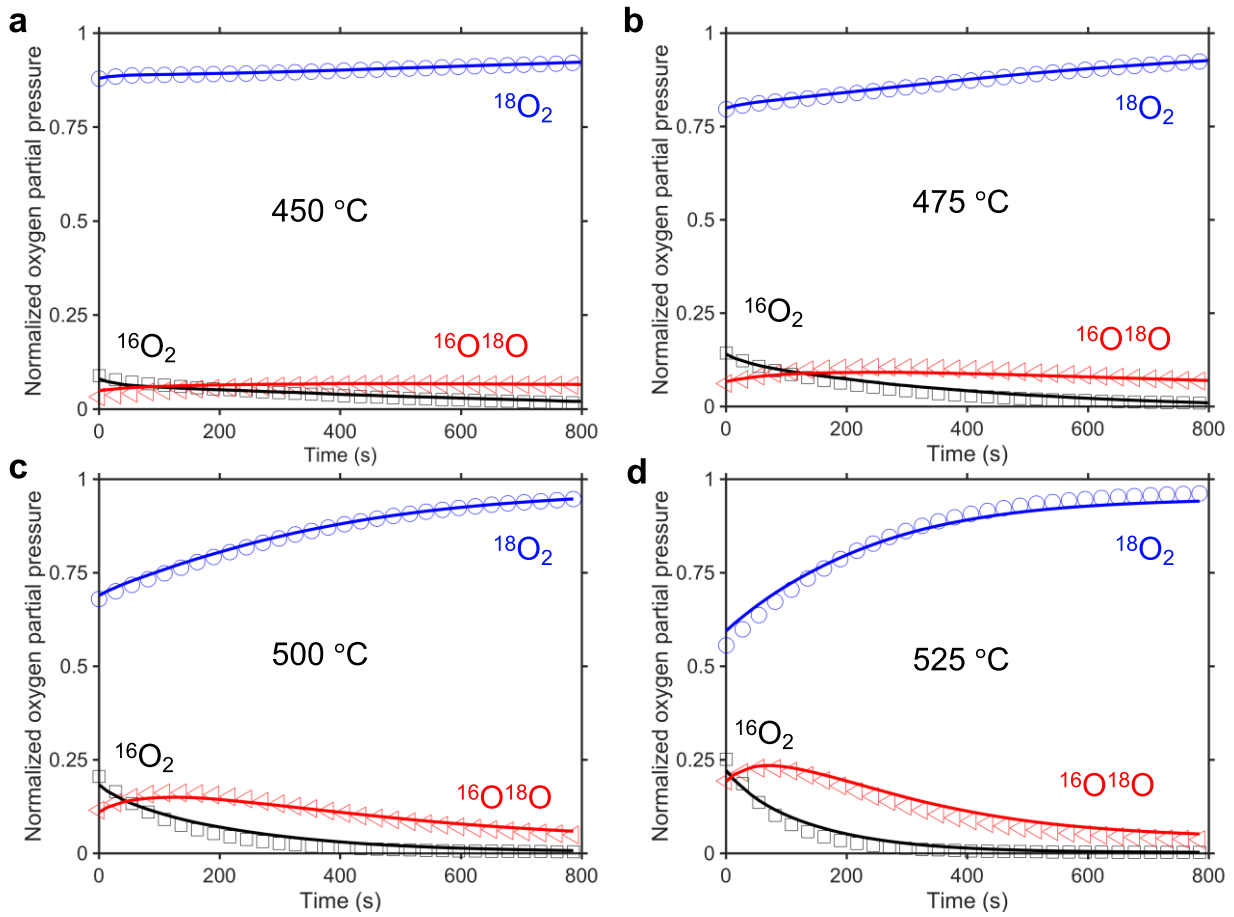

Figure S12. Normalized transient response curves for isotopic oxygen exchange on Fe-LNO at an oxygen partial pressure of 0.02 atm and a temperature of 450 °C (a), 475 °C (b), 500 °C (c), and 525 °C (d). The symbols and solid lines refer to the experimental and model fitted data, respectively.

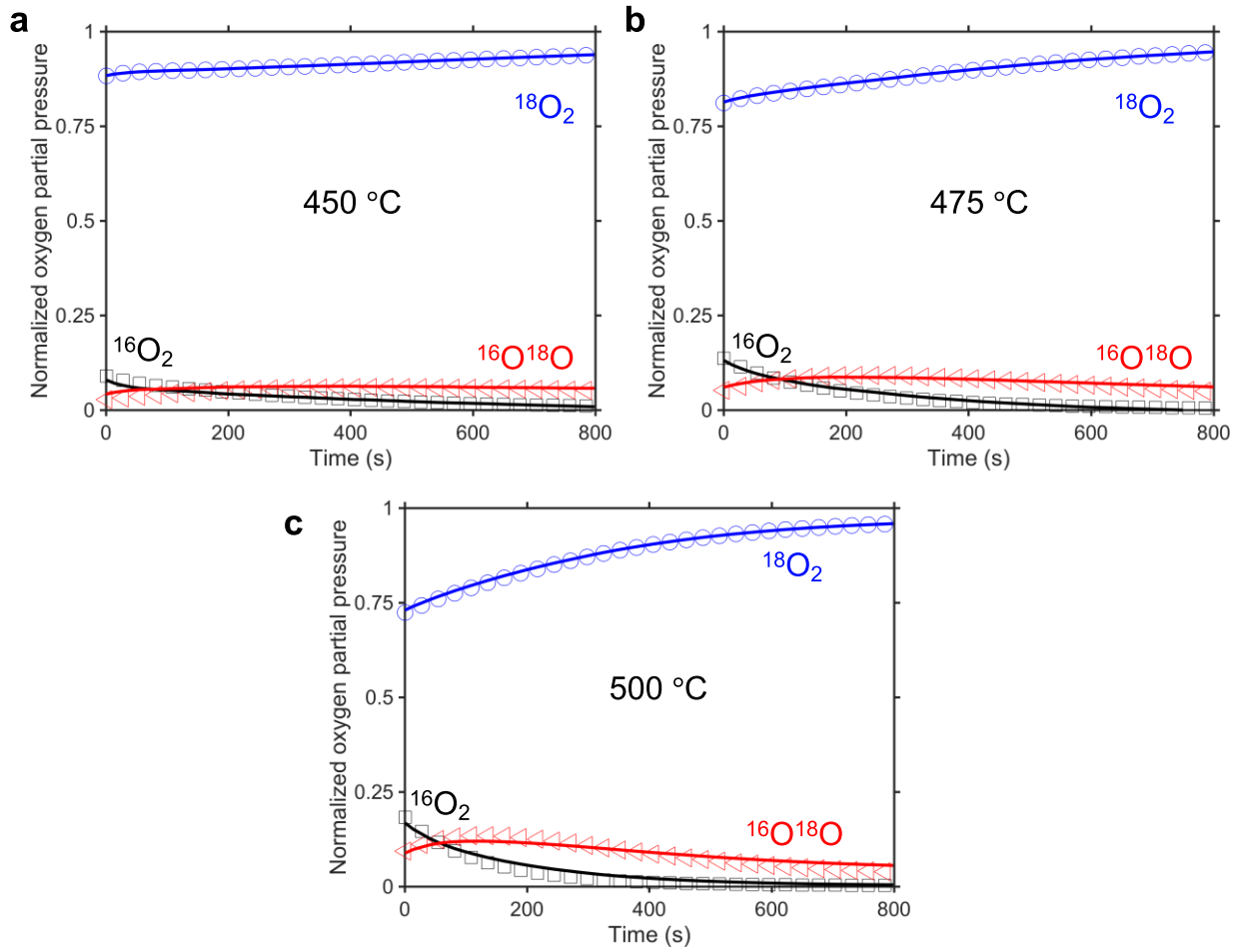

Figure S13. Normalized transient response curves for isotopic oxygen exchange on LNO at an oxygen partial pressure of 0.02 atm and a temperature of 450 °C (a), 475 °C (b), and 500 °C (c). The symbols and solid lines refer to the experimental and model fitted data, respectively.

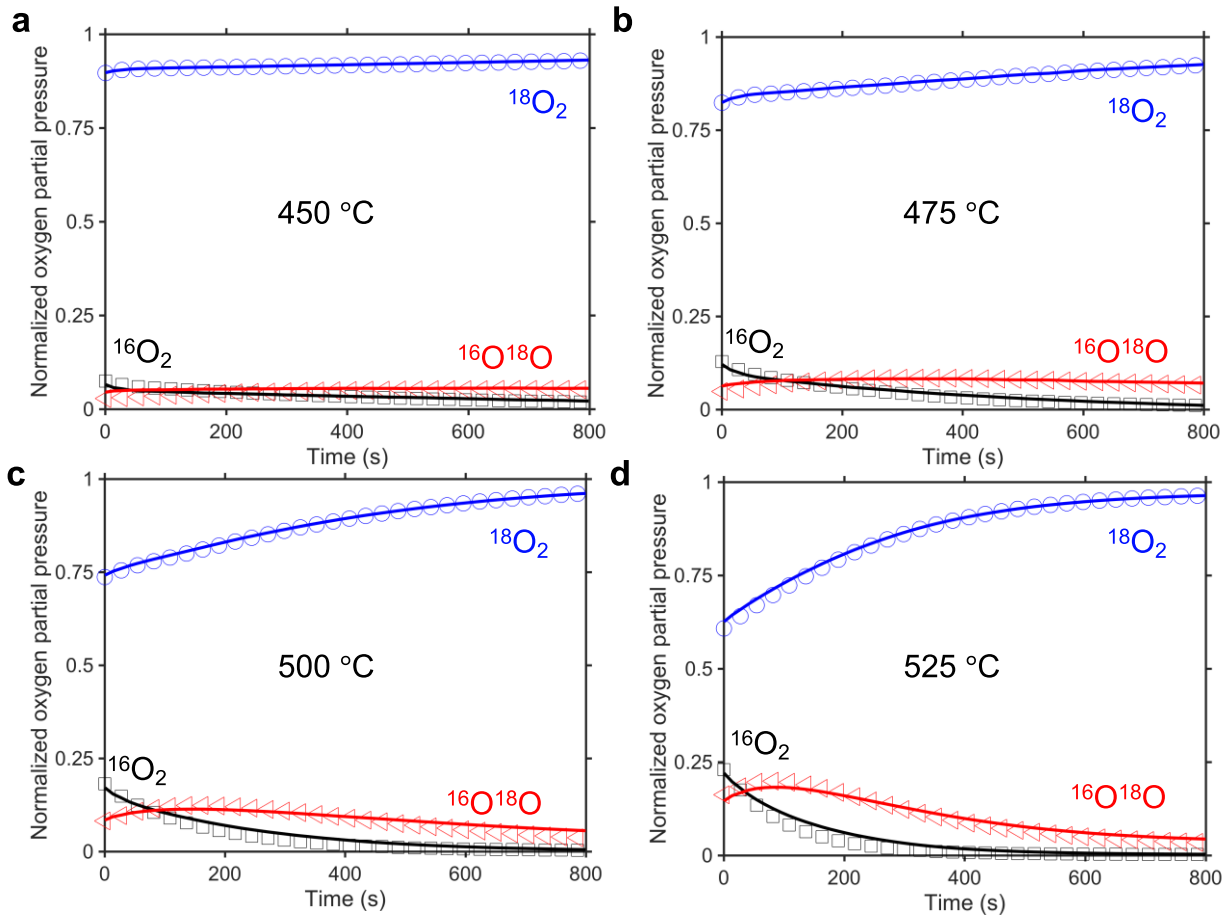

Figure S14. Normalized transient response curves for isotopic oxygen exchange on Cu-LNO at an oxygen partial pressure of 0.02 atm and a temperature of 450 °C (a), 475 °C (b), 500 °C (c), and 525 °C (d). The symbols and solid lines refer to the experimental and model fitted data, respectively.

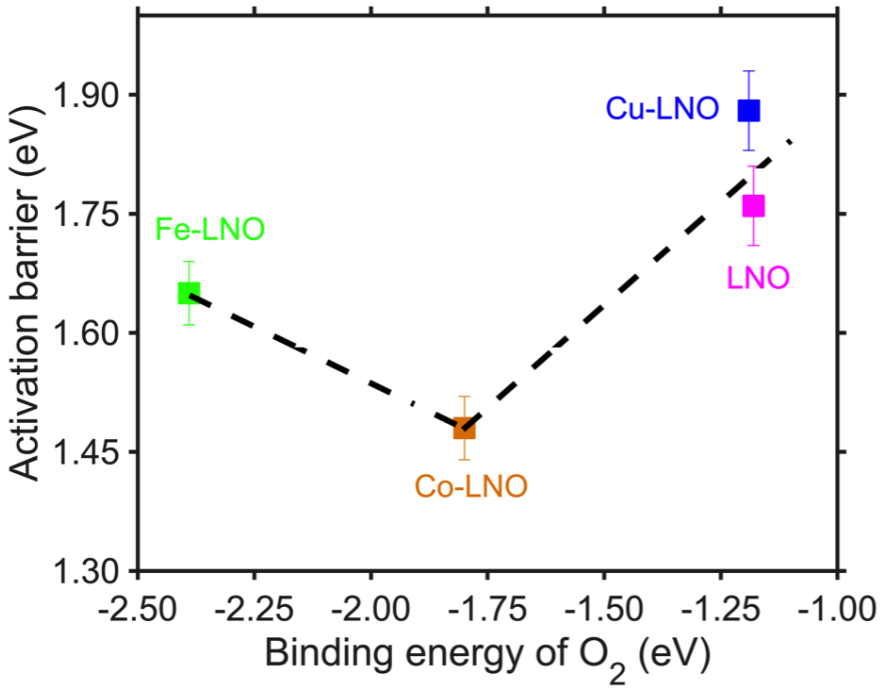

Figure S15. A reversed "volcano"-type relationship for the barrier of the rate-limiting step extracted from the experimental fitted model as a function of the binding energy of O_2 on a surface oxygen vacancy on R-P oxides.

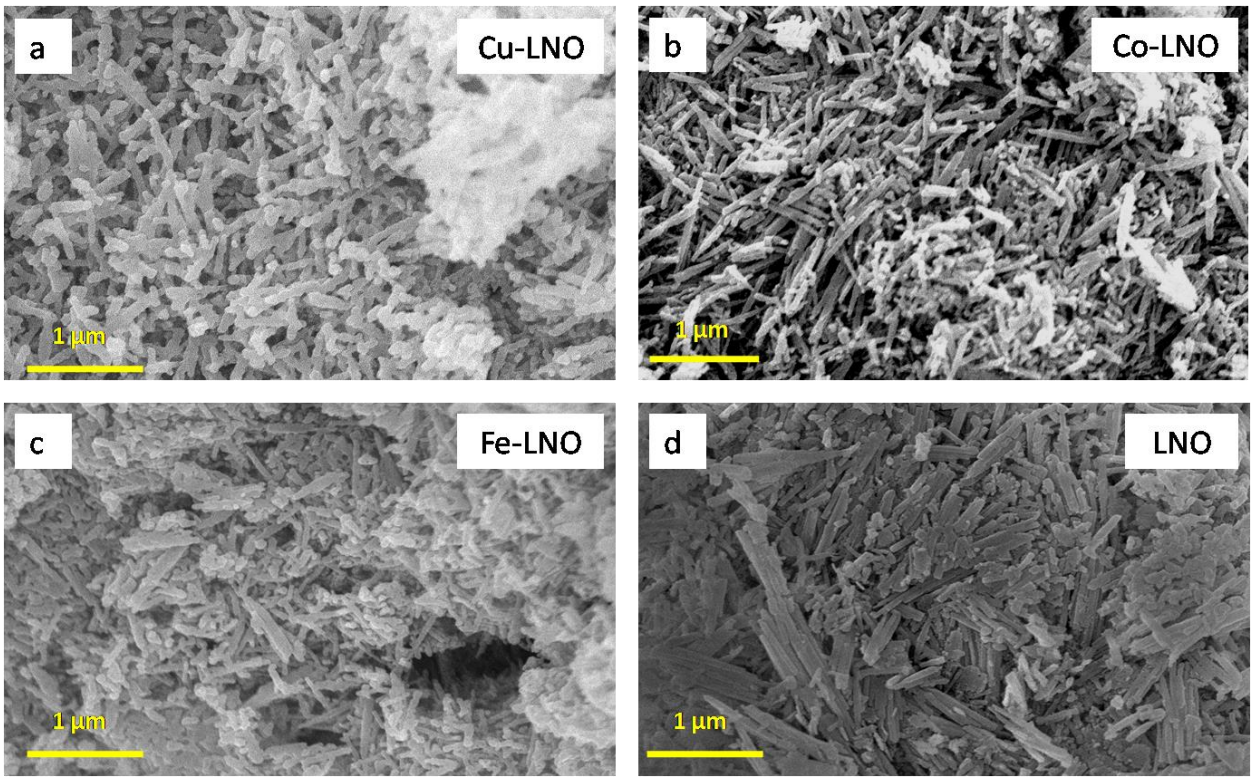

Figure S16. Post-reaction SEM images of a) Cu-LNO, b) Co-LNO, c) Fe-LNO, and d) LNO nanorods.

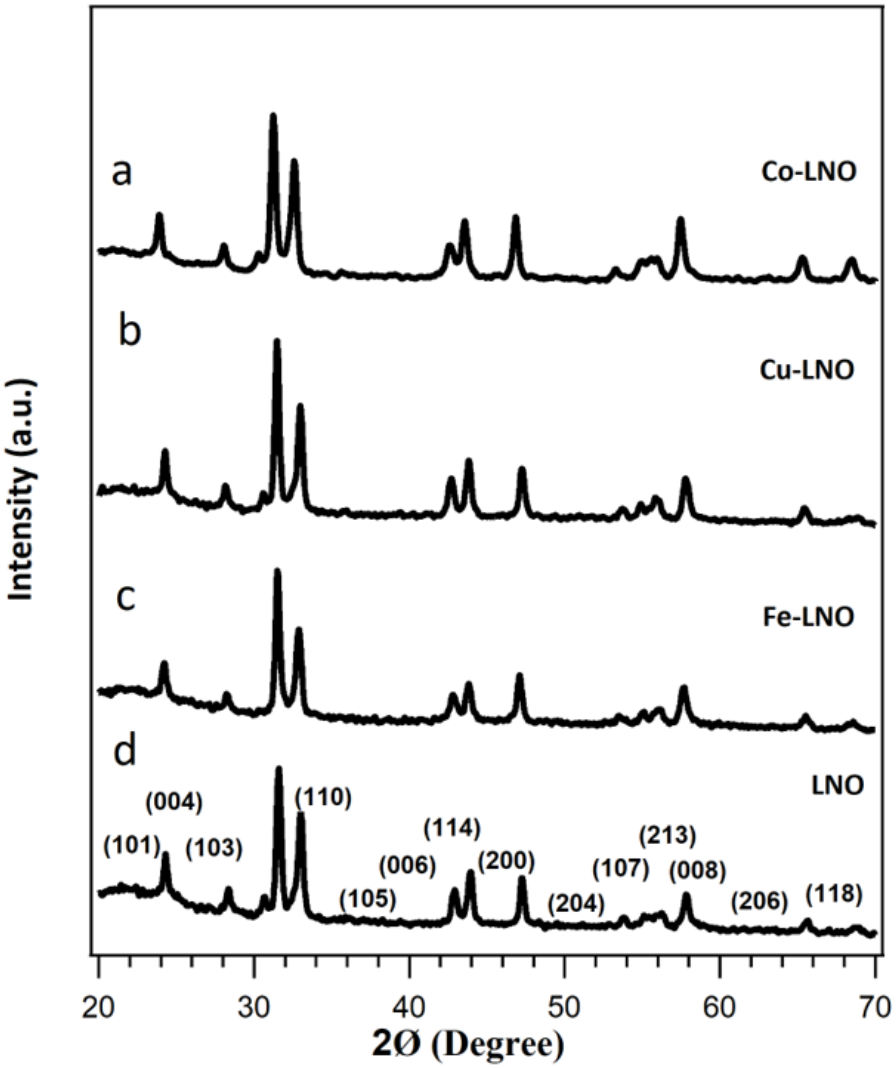

Figure S17. Post-reaction XRD characterization of a) Co-LNO, b) Cu-LNO, c) Fe-LNO, and d) LNO.

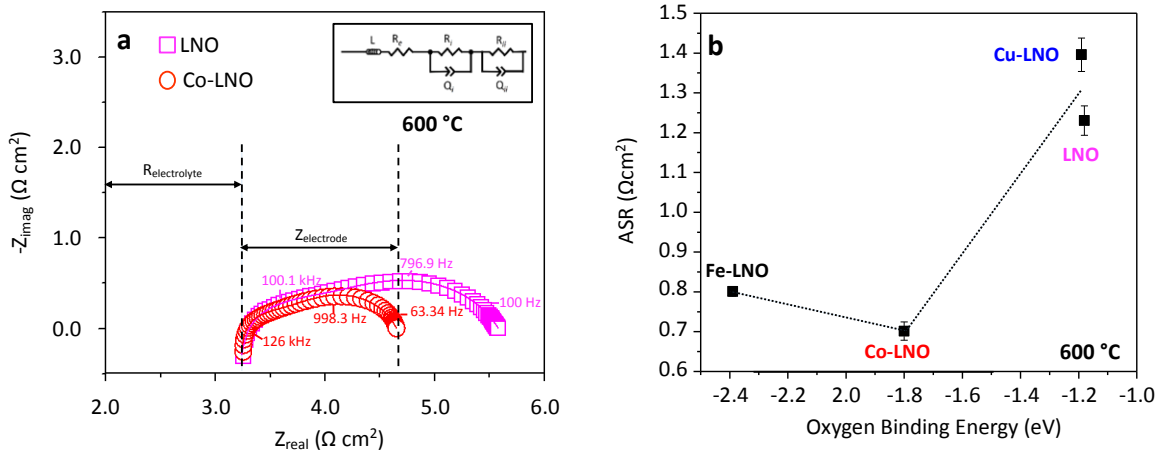

Figure S18. (a) Impedance spectra for R-P oxides–YSZ | YSZ | YSZ–R-P oxides symmetric cells operating at pO_2 = 1 atm and 600 ℃. The equivalent circuit used to fit the polarization resistance curves is shown as an inset. (b) Area specific resistance for R-P oxides–YSZ | YSZ | YSZ–R-P oxides symmetric cells as function of O_2 binding energy on a surface oxygen vacancy at 600 ℃.

In the spectra (Fig S18a), $R_{electrolyte}$ refers to the ohmic losses induced by the electrolyte, while $Z_{electrode}$ refers to the polarization resistances from the electrodes, obtained by normalizing the raw impedance data using the electrode geometrical area (S = 0.1 cm^2). The $Z_{electrode}$ of the electrochemical cells containing R-P oxides is fitted using an equivalent circuit of the type $LR_e(R_iQ_i)(R_{ii}Q_{ii})$ (Fig. S18, inset). Here L denotes the inductance caused by the electrical connections and R_e represents the ohmic resistance from the YSZ electrolyte. The circuit elements composed of two resistances in parallel with two constant phase elements (R_iQ_i and $R_{ii}Q_{ii}$) are related to the $Z_{electrode}$ occurring at high (R_iQ_i) and low frequency ($R_{ii}Q_{ii}$) ranges in the electrode. The area specific resistances (ASRs) are calculated as $ASR = R_x/2$ ($x = i$ or ii).

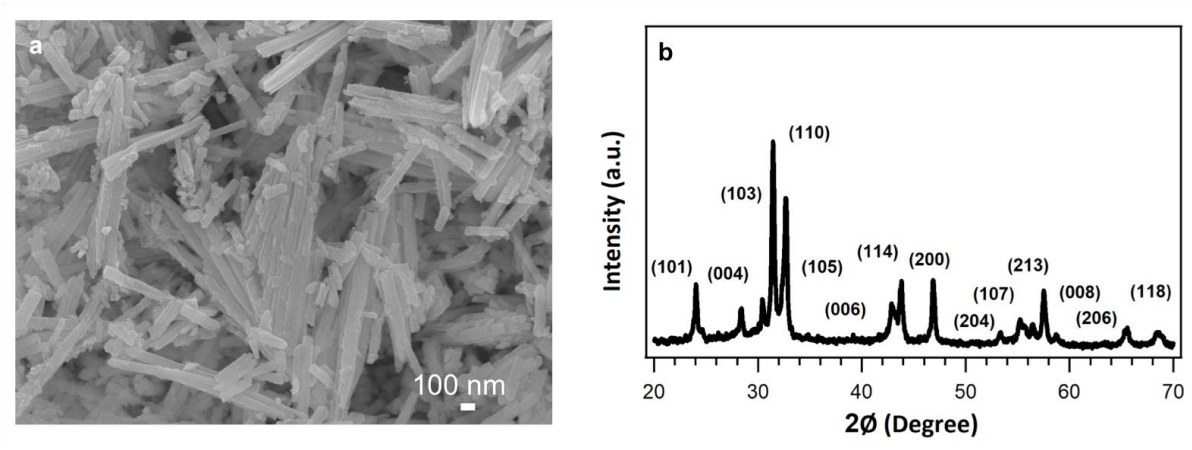

Figure S19. SEM image (a) and XRD spectrum (b) of as-synthesized $La_2Ni_{0.75}Co_{0.25}O_{4+\delta}$.

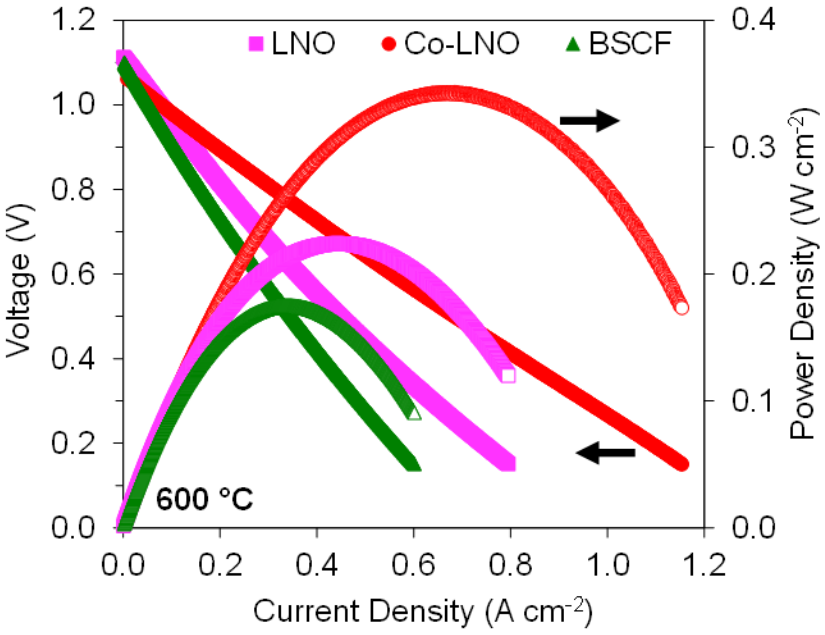

Figure S20. Electrochemical performance of SOFCs containing LNO nanorods, Co-LNO nanorods, and $Ba_{0.5}Sr_{0.5}Co_{0.8}Fe_{0.2}O_3$ (BSCF) at 600 ℃.

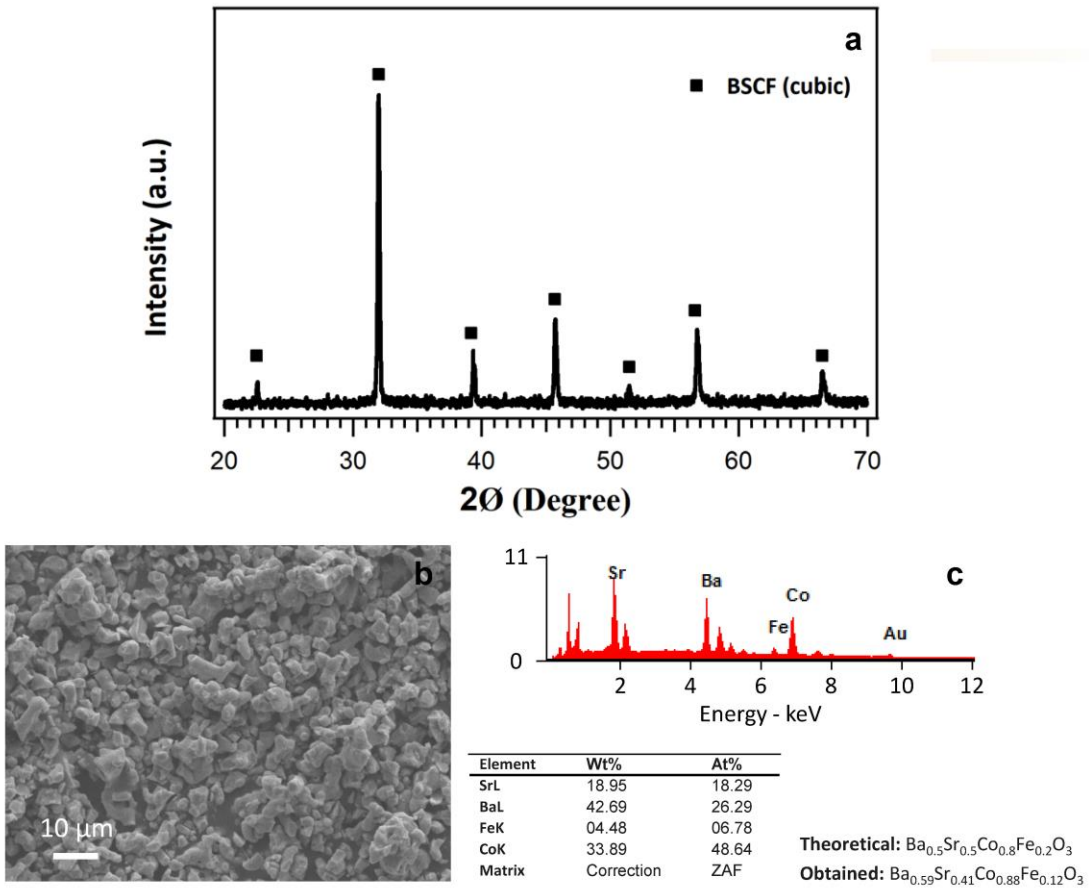

Figure S21. XRD spectrum (a), SEM image (b), and EDS spectrum (c) of the as-synthesized $Ba_{0.5}Sr_{0.5}Co_{0.8}Fe_{0.2}O_3$.

Synthesis of $Ba_{0.5}Sr_{0.5}Co_{0.8}Fe_{0.2}O_3$ (BSCF) is adopted from literature.[29] It involves dissolving appropriate amounts of the metal salts (barium, strontium, and cobalt nitrates; iron chloride) in de-ionized water. The pH of the solution is adjusted to ~3 by adding HCl. An aqueous solution of ammonium oxalate is added dropwised to the salt solution and stirred until the solids are precipitated from the solution. The solids are separated via centrifugation and the resultant precipitate is dried at 250 ℃ for 8 h, followed by calcination in air at 1050 ℃ for 5 h.

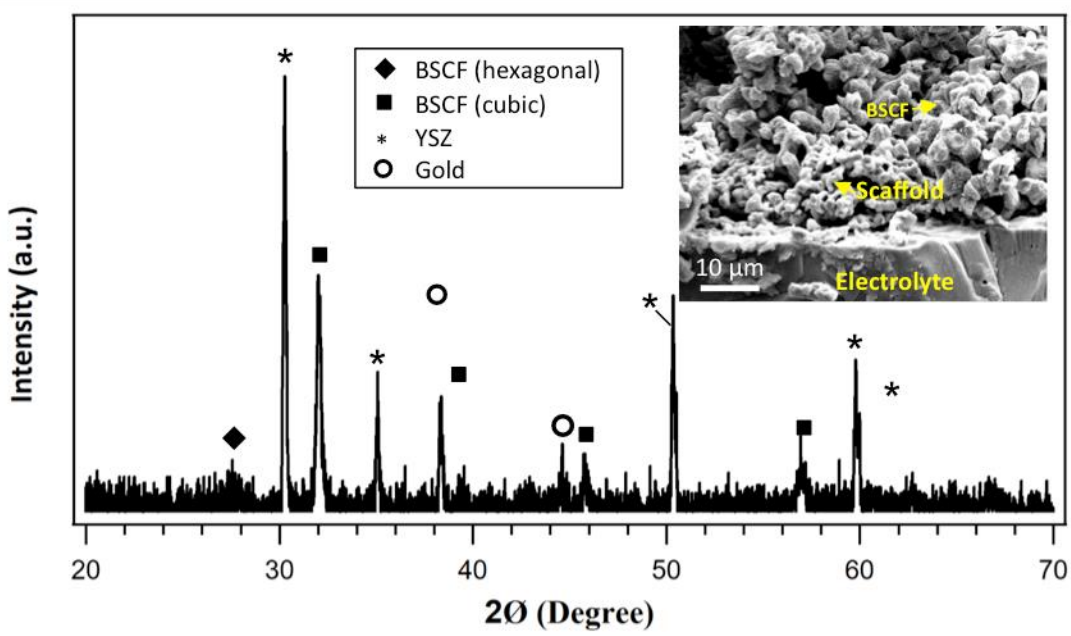

Figure S22. Post-reaction XRD/SEM characterization of BSCF containing electrodes.

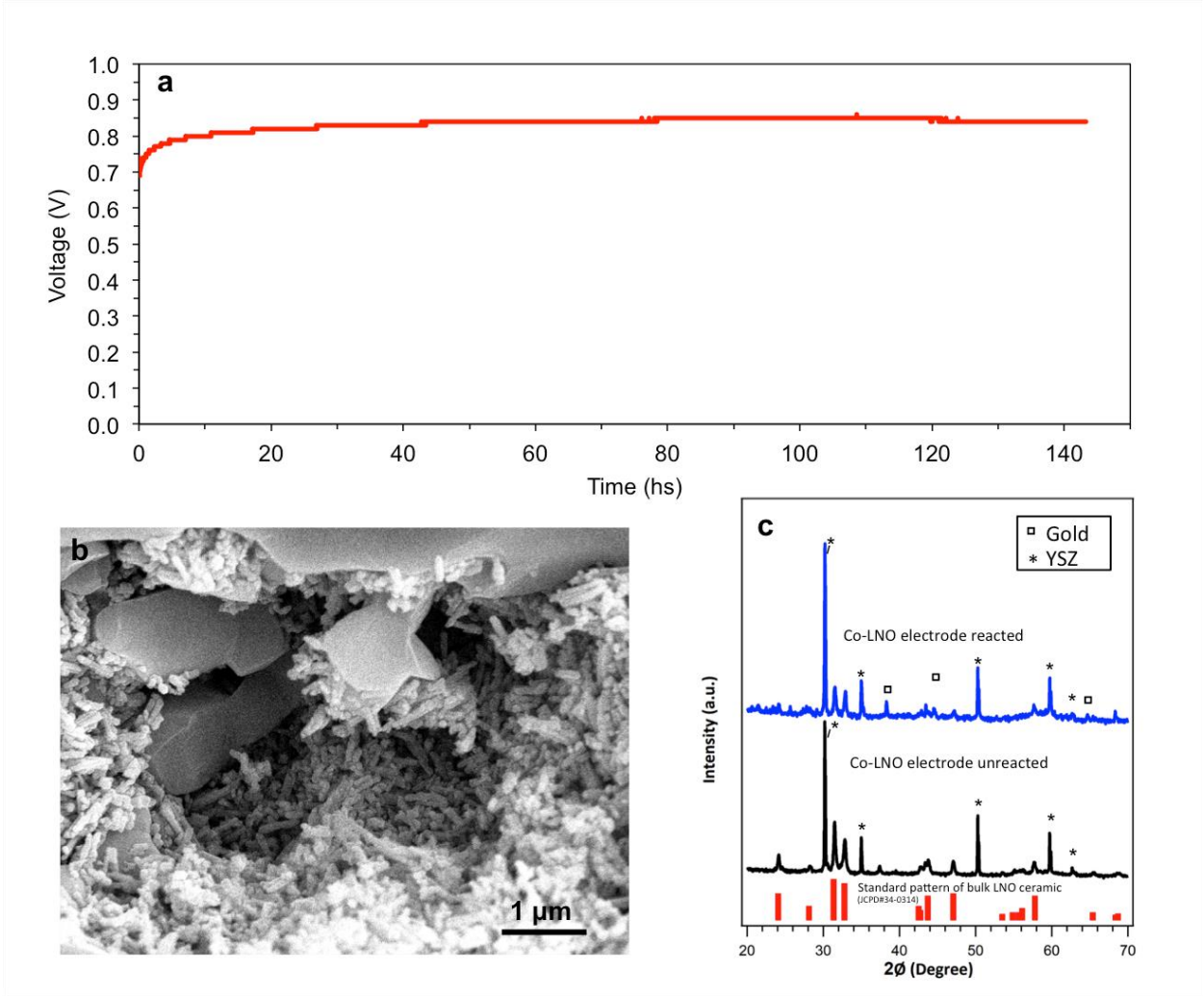

Figure S23. Stability test for anode-supported SOFCs containing Co-LNO nanostructures at the cathode. (a) Galvanostatic test (at 720 mA cm^{-2}) measured over 140 h at 700 ℃. (b) SEM images of SOFC cathode containing Co-LNO nanorods after 140 hours of operation. (c) XRD spectra of SOFC cathode after electrochemical studies (blue), SOFC cathode before reaction (black), and standard bulk LNO (red).

Table S1. Calculated energy barriers and Gibbs free energy change for surface lattice O diffusion into an interstitial site and O_2 dissociation on surface O vacancy on B-site terminated (001) surface of R-P oxides at 500 ℃ and 0.21 atm. The values for the undoped oxides are adopted from the literature.[15]

	$O_O^X + V_i \rightarrow V_O^{\bullet\bullet} + O_i$		$O_2 + V_O^{\bullet\bullet} + * \rightarrow O* + O_O^X$	
	E_{TS}(eV)	ΔG(eV)	E_{TS}(eV)	ΔG(eV)
La_2MnO_4	1.30	0.39	-1.35	-2.31
La_2FeO_4	1.44	0.13	-0.85	-1.77
La_2CoO_4	1.15	-0.04	0.21	-0.49
La_2NiO_4	1.61	0.32	1.90	1.76
$La_2Ni_{0.5}Al_{0.5}O_4$	1.71	0.27	-2.58	-2.84
$La_2Ni_{0.5}Mn_{0.5}O_4$	1.79	0.21	-0.75	-1.97
$La_2Ni_{0.5}Fe_{0.5}O_4$	1.57	0.29	-0.21	-1.21
$La_2Ni_{0.5}Co_{0.5}O_4$	1.14	0.18	0.56	-0.12
$La_2Ni_{0.5}Cu_{0.5}O_4$	1.96	1.28	1.99	1.83

Table S2. Calculated binding energies of O adatom (BE_O), O_2 on a surface O vacancy (BE_{O_2}), and surface O vacancy formation energies ($E_{V_O^{\bullet\bullet}}$) on B-site terminated (001) surface of R-P oxides. $E_{V_O^{\bullet\bullet}}$ is calculated with respect to a half O_2 in gas phase with the consideration of entropic contribution at 500 ℃ and 0.21 atm. The values for the undoped oxides are adopted from the literature.[15]

	BE_O (eV)	BE_{O_2} (eV)	$E_{V_O^{\bullet\bullet}}$ (eV)
La_2MnO_4	-0.61	-3.47	3.35
La_2FeO_4	-0.43	-2.61	2.08
La_2CoO_4	0.15	-2.06	1.38
La_2NiO_4	1.35	-1.18	0.33
$La_2Ni_{0.5}Al_{0.5}O_4$	-0.83	-4.67	4.36
$La_2Ni_{0.5}Mn_{0.5}O_4$	-0.42	-2.99	3.04
$La_2Ni_{0.5}Fe_{0.5}O_4$	-0.03	-2.39	1.92
$La_2Ni_{0.5}Co_{0.5}O_4$	0.37	-1.80	1.23
$La_2Ni_{0.5}Cu_{0.5}O_4$	1.22	-1.19	0.14

Table S3. Literature reported performances for various YSZ-based SOFCs at intermediate temperatures.

Literature	Cell Composition anode/(electrolyte)/cathode	Temperature (°C)	Power Density (W/cm^2)
This work	**Ni-YSZ/(YSZ_15 μm)/YSZ-Co-doped LNO**	**550**	**0.2**
		600	**0. 34**
	Ni-YSZ/(YSZ_15 μm)/YSZ-BSCF	**550**	**0.08**
		600	**0.17**
Xu et al., (2005) [30]	Ni-SDC/(YSZ)/ $Y_{0.25}Bi_{0.75}O_{1.5}$ -Ag	600	~0.093
Moon et al., (2008) [31]	Ni-YSZ/(YSZ)/$La_{0.8}Sr_{0.2}MnO_3$-YSZ	600	~0.1
Liu et al., (2004) [32]	Ni-GDC/(YSZ)/LSM-GDC/LSM-LSC-GDC/LSC-GDC	600	0.138
Tsai & Barnett., (1997) [33]	Ni-YSZ/(YSZ)/$La_{0.8}Sr_{0.2}MnO_3$	550	0. 056
		600	0. 1
		650	0. 17
Kan & Lee (2010) [34]	Ni-YSZ/(YSZ)/$La_{0.8}Sr_{0.2}MnO_3$-YSZ	650	0.39
	Sn-doped Ni-YSZ/(YSZ)/ $La_{0.8}Sr_{0.2}MnO_3$-YSZ	650	0.41
Leng et al. (2004) [35]	Ni-YSZ/(YSZ)/LSM-YSZ/ $La_{0.72}Sr_{0.18}MnO_3$	650	0.14
Tsai et al., (1997) [36]	Ni-YSZ/YDC/(YSZ/YDC)/$La_{0.85}Sr_{0.15}MnO_3$-YSZ	500	~0.043
		550	~0.09
		600	~0.154
Kim et al., (2016) [37]	Ni-YSZ/(YSZ/GDC)/ $La_{0.6}Sr_{0.4}Co_{0.2}Fe_{0.8}O_3$-GDC	600	0.2
Choi et al., (2014) [38]	Ni– GDC/(YSZ/GDC)/ $La_{0.6}Sr_{0.4}Co_{0.2}Fe_{0.8}O_3$–GDC	600	0.208
Lim & Virkar (2009) [39]	NiO-YSZ/(YSZ/GDC)/ $LaCoO_3$ -GDC	650	~0.14
Cho et al., (2011) [40]	Ni-YSZ/(YSZ_330nm)/GDC_6 μm)/ $La_{0.5}Sr_{0.5}CoO_3$ -GDC*	650	0.18

* Reported low open circuit voltage (OCV > 0.67V at 750 °C)

References

(1) Wang, L.; Maxisch, T.; Ceder, G., *Phys. Rev. B* **2006,** *73*, 195107.

(2) Henkelman, G.; Uberuaga, B. P.; Jonsson, H., *J. Chem. Phys.* **2000,** *113*, 9901-9904.

(3) Henkelman, G.; Jonsson, H., *J. Chem. Phys.* **2000,** *113*, 9978-9985.

(4) Gu, X. K.; Liu, B.; Greeley, J., *ACS Catal.* **2015,** *5*, 2623-2631.

(5) Khavryuchenko, O. V.; Peslherbe, G. H., *Chemcatchem* **2016,** *8*, 3156-3160.

(6) Zhu, C.; Liang, J. X.; Wang, B. J.; Zhu, J.; Cao, Z. X., *Phys. Chem. Chem. Phys.* **2012,** *14*, 12800-12806.

(7) Klier, K.; Novakova, J.; Jiru, P., *J. Catal.* **1963,** *2*, 479-484.

(8) Huang, Y. L.; Pellegrinelli, C.; Wachsman, E. D., *ACS Catal.* **2016,** *6*, 6025-6032.

(9) Doornkamp, C.; Clement, M.; Ponec, V., *J. Catal.* **1999,** *182*, 390-399.

(10) Ivanov, D. V.; Sadovskaya, E. M.; Pinaeva, L. G.; Isupova, L. A., *J. Catal.* **2009,** *267*, 5-13.

(11) Rochoux, M.; Guo, Y.; Schuurman, Y.; Farrusseng, D., *Phys. Chem. Chem. Phys.* **2015,** *17*, 1469-1481.

(12) Boreskov, G. K., *Discuss. Faraday Soc.* **1966**, 263-&.

(13) Ma, X. F.; Carneiro, J. S. A.; Gu, X. K.; Qin, H.; Xin, H. L.; Sun, K.; Nikolla, E., *ACS Catal.* **2015,** *5*, 4013-4019.

(14) Das, A.; Xhafa, E.; Nikolla, E., *Catal. Today* **2016,** *277*, 214-226.

(15) Gu, X. K.; Nikolla, E., *ACS Catal.* **2017,** *7*, 5912-5920.

(16) Campbell, C. T.; Sprowl, L. H.; Arnadottir, L., *J. Phys. Chem. C* **2016,** *120*, 10283-10297.

(17) Sayers, R.; De Souza, R. A.; Kilner, J. A.; Skinner, S. J., *Solid State Ionics* **2010,** *181*, 386-391.

(18) Nakamura, T.; Oike, R.; Ling, Y. H.; Tamenori, Y.; Amezawa, K., *Phys. Chem. Chem. Phys.* **2016,** *18*, 1564-1569.

(19) Boehm, E.; Bassat, J. M.; Dordor, P.; Mauvy, F.; Grenier, J. C.; Stevens, P., *Solid State Ionics* **2005,** *176*, 2717-2725.

(20) Tsvetkov, N.; Chen, Y.; Yildiz, B., *J. Mater. Chem. A* **2014,** *2*, 14690-14695.

(21) Suzuki, C.; Kawai, J.; Takahashi, M.; Vlaicu, A. M.; Adachi, H.; Mukoyama, T., *Chem. Phys.* **2000,** *253*, 27-40.

(22) Rojas, M.; Fierro, J.; Tejuca, L.; Bell, A. T., *J. Catal.* **1990,** *124*, 41-51.

(23) Ertl, G.; Hierl, R.; Knözinger, H.; Thiele, N.; Urbach, H., *Appl. Surf. Sci.* **1980,** *5*, 49-64.

(24) Burriel, M.; Wilkins, S.; Hill, J. P.; Muñoz-Márquez, M. A.; Brongersma, H. H.; Kilner, J. A.; Ryan, M. P.; Skinner, S. J., *Energy Environ. Sci.* **2014,** *7*, 311-316.

(25) Ning, X.; Wang, Z.; Zhang, Z., *Sci. Rep.* **2015,** *5*, 8460.

(26) Turner, N.; Single, A., *Surf. Interface Anal.* **1990,** *15*, 215-222.

(27) McIntyre, N.; Cook, M., *Anal. Chem.* **1975,** *47*, 2208-2213.

(28) Liang, Q.; Gao, L.; Li, Q.; Tang, S.; Liu, B.; Yu, Z., *Carbon* **2001,** *39*, 897-903.

(29) Toprak, M. S.; Darab, M.; Syvertsen, G. E.; Muhammed, M., *Int. J. Hydrogen Energy* **2010,** *35*, 9448-9454.

(30) Xu, X.; Xia, C.; Huang, S.; Peng, D., *Ceram. Int.* **2005,** *31*, 1061-1064.

(31) Moon, H.; Kim, S. D.; Hyun, S. H.; Kim, H. S., *Int. J. Hydrogen Energy* **2008,** *33*, 1758-1768.

(32) Liu, Y.; Compson, C.; Liu, M., *J. Power Sources* **2004,** *138*, 194-198.

(33) Tsai, T.; Barnett, S. A., *Solid State Ionics* **1997,** *93*, 207-217.

(34) Kan, H.; Lee, H., *Appl. Catal. B* **2010,** *97*, 108-114.

(35) Leng, Y.; Chan, S.; Khor, K.; Jiang, S., *Int. J. Hydrogen Energy* **2004,** *29*, 1025-1033.

(36) Tsai, T.; Perry, E.; Barnett, S., *J. Electrochem. Soc.* **1997,** *144*, L130-L132.

(37) Kim, H. J.; Kim, M.; Neoh, K. C.; Han, G. D.; Bae, K.; Shin, J. M.; Kim, G.-T.; Shim, J. H., *J. Power Sources* **2016,** *327*, 401-407.

(38) Choi, H.; Cho, G. Y.; Cha, S.-W., *Int. J. Precis. Eng. Man.* **2014,** *1*, 95-99.

(39) Lim, H.-T.; Virkar, A. V., *J. Power Sources* **2009,** *192*, 267-278.

(40) Cho, S.; Kim, Y.; Kim, J.-H.; Manthiram, A.; Wang, H., *Electrochim. Acta* **2011,** *56*, 5472-5477.